SEISMIC WAVEFIELD SIMULATION WITH IRREGULAR SURFACE TOPOGRAPHY AND GRAPHIC PROCESSING UNIT (GPU) IMPLEMENTATION

XIAOBO LIU[1], JINGYI CHEN[1*], HAIQIANG LAN[2] and ZHENCONG ZHAO[1]

[1] Seismic Anisotropy Group, Department of Geosciences, The University of Tulsa, Tulsa, OK 74104, U.S.A. jingyi-chen@utulsa.edu
[2] Key Laboratory of Earth and Planetary Physics, Institute of Geology and Geophysics, Chinese Academy of Sciences, Beijing 100029, P.R. China.

(Received August 24, 2017; revised version accepted July 30, 2018)

ABSTRACT

Liu, X.B., Chen, J.Y., Lan, H.Q. and Zhao, Z.C., 2018. Seismic wavefield simulation with irregular surface topography and Graphic Processing Unit (GPU) implementation. *Journal of Seismic Exploration*, 27: 445-472.

Seismic wavefield simulation in the presence of surface topography provides important information for characterizing seismic wave propagation. Based on the boundary-conforming grid method, we first transform both elastic wave equations in second-order formulation and free surface boundary condition in first order system from Cartesian coordinates to curvilinear coordinates. Then, the convolutional perfectly matched layer (CPML) boundary condition is applied to absorb the outgoing seismic waves at the edges of the truncated model. The test results (e.g., wavefield snapshots and seismograms) show that our numerical algorithms can effectively simulate seismic wave propagation in a model with rough topography, and CPML is more efficient than perfectly matched layer (PML) boundary condition in suppressing artificial reflections. In addition, the finite-difference algorithms on a single Graphic Processing Unit (GPU) are used to accelerate seismic numerical modeling in both elastic isotropic and anisotropic media. Compared with the conventional CPU version, the GPU implementation greatly reduces the computational cost.

KEY WORDS: wavefield simulation, surface topography, finite-difference, convolutional perfectly matched layer, Graphic Processing Unit, GPU.

0963-0651/18/$5.00 © 2018 Geophysical Press Ltd.

INTRODUCTION

In land seismic surveys, seismic signals are usually recorded by geophones at the surface of the earth. The earth's complex topography (e.g., mountain and basin areas) makes it necessary for us to simulate seismic wave propagation in a medium with irregular topography. In the last four decades, there have mainly been two kinds of schemes to deal with a model with rough topography: (1) a fictitious layer is added above the free surface (Alterman and Karal, 1968; Vidale and Clayton, 1986); (2) derivatives are substituted to the free surface without any fictitious layer above the free surface (e.g., composed approximation, remedy scheme and boundary-conforming grid) (Ilan et al., 1975; Ilan, 1978; Nielsen et al., 1994; Nilsson et al., 2007; Appelö and Petersson, 2009; Lan and Zhang, 2011; Sofronov et al., 2015). In our study, we use the boundary-conforming grid method because of its easy implementation (Appelö and Petersson, 2009). Among the numerical algorithms available, the spectral element and finite element methods satisfy the free surface naturally but suffer from high computational costs or inaccuracy problems (Komatitsch and Tromp, 1999; Tessmer et al., 1992). The combination of the finite element and finite-difference methods makes an algorithm suitable for the complex near surface part but it still suffers from high computational costs (Galis et al., 2008; Lisitsa et al., 2016). Compared with spectral element, finite element and hybrid finite-difference methods, the finite-difference method became more effective for modeling seismic wave propagation with free surface topography since Nilsson et al. (2007) proposed a boundary modified difference approximation in the Cartesian system. This new boundary modified difference method makes numerical computing with an irregular free surface easier, more flexible and stable. Appelö and Petersson (2009) extended this stable discretization into curvilinear coordinates to handle the free surface boundary conditions in elastic isotropic media. Lan and Zhang (2011) further extended this scheme to seismic wavefield simulation in anisotropic media. Compared with only transforming the vertical coordinate in the curvilinear scheme proposed by Tarrass et al. (2011), both vertical and lateral coordinates are transformed from the Cartesian to curvilinear coordinates. This kind of transformation can deal with more complex topography. However, the absorbing boundary condition (Cerjan et al., 1985; Chen et al., 2010) used in their studies was not working well to suppress the unwanted reflections from the boundaries of the model.

Bérenger (1994) first introduced the perfectly matched layer (PML) boundary condition and proved its efficiency compared to classic boundary conditions. It is widely used in seismic numerical modeling since it was proposed (Abarbanel et al., 1999; Collino and Tsogka, 2001; Komatitsch and Tromp, 2003). Then, in order to improve the behavior of PML at grazing incidence, a convolutional perfectly matched layer (CPML) was proposed by Roden and Gedney (2000). Komatitsch and Martin (2007) further proved that CPML has better behavior than PML at grazing incidence for the differential seismic wave equations, especially for the case of a source located close to the edge. Lan et al. (2016) applied the perfectly matched layer (PML) boundary condition to 2D elastic isotropic media with rough

topography. Here, we will adopt the CPML to both 2D elastic isotropic and anisotropic media in order to take advantage of its significant absorbing performance. CPML has proved to be highly effective at absorbing artificial reflections and surface waves since it was proposed for electromagnetic media (Roden and Gedny, 2000). Usually, CPML is used in first order velocity-stress equations (Drossaert and Giannopoulos, 2007; Martin et al., 2008). Li and Matar (2010) extended it into second-order elastodynamic equations in the Cartesian coordinate system. But they did not deal with the need to suppress artificial scattered waves at the free surface. In this study, we will implement both CPML and free surface boundary conditions for simulating seismic wavefield propagation in elastic isotropic and anisotropic media with an irregular free surface in the curvilinear coordinate system. The elastic wave equations and free surface boundary condition are second-order and first order formulations, respectively. The numerical results show that CPML is successfully applied to seismic wave equations with an irregular free surface in the curvilinear coordinate system.

Another limitation of seismic wavefield simulation is that it suffers from high computational costs. To solve this problem, geophysicists not only optimize the algorithm but also adopt new computing technologies. In recent years, Graphic Processing Unit (GPU) parallel computing has gained more and more popularity in many scientific fields, such as physics, geophysics, and computer science (Preis, 2011; Panetta et al., 2009). A number of geophysical problems have been solved using GPUs, such as wavefield simulation (Michéa and Komatisch, 2010), reverse time migration (Micikevicius, 2009; Abdelkhalek et al., 2009; Liu et al., 2012) and full waveform inversion (Shin et al., 2014; Yang et al., 2015; Liu et al., 2015). In this paper, we carry out parallel computing using a NVIDIA® GPU card (Tesla C2075) to accelerate the numerical simulation of seismic wave propagation. CPU and GPU runtimes are compared to show parallel computing efficiency.

This paper is organized as follows. First, we transform the 2D elastic wave equation and irregular free surface boundary condition from the Cartesian coordinate system to the curvilinear coordinate system. Second, we incorporate a CPML boundary condition to the wave equations in curvilinear coordinates to absorb the outgoing waves at the boundaries of the model. Finally, through elastic elongated model studies in seismic wavefield snapshots, seismograms and energy decay, we show that CPML has better absorbing behavior than PML, and GPU processing effectively accelerates seismic wavefield simulation.

SEISMIC NUMERICAL MODELING WITH IRREGULAR FREE SURFACE

In the Cartesian coordinates, the 2D elastic wave equations in the time domain (Lan et al., 2011) are given by

$$\rho \frac{\partial^2 u}{\partial t^2} = \frac{\partial}{\partial x}\left(c_{11}\frac{\partial u}{\partial x} + c_{13}\frac{\partial v}{\partial z} \right) + \frac{\partial}{\partial z}\left(c_{44}\frac{\partial u}{\partial z} + c_{44}\frac{\partial v}{\partial x} \right) \quad , \tag{1a}$$

$$\rho \frac{\partial^2 \mathrm{v}}{\partial t^2} = \frac{\partial}{\partial x}\left(c_{44}\frac{\partial v}{\partial x} + c_{44}\frac{\partial u}{\partial z} \right) + \frac{\partial}{\partial z}\left(c_{33}\frac{\partial v}{\partial z} + c_{13}\frac{\partial u}{\partial x} \right) \quad , \tag{1b}$$

where $c_{ij}(x,z)$ are the elastic parameters; u and v are the displacements along the x and z directions; $\rho(x,z)$ is the density of the material.

At the surface, the free surface boundary condition in the Cartesian coordinates (Lan et al., 2011) is expressed by

$$\begin{bmatrix} c_{11}\frac{\partial u}{\partial x} + c_{13}\frac{\partial v}{\partial z} & c_{44}\frac{\partial u}{\partial z} + c_{44}\frac{\partial v}{\partial x} \\ c_{44}\frac{\partial v}{\partial x} + c_{44}\frac{\partial u}{\partial z} & c_{33}\frac{\partial v}{\partial z} + c_{13}\frac{\partial u}{\partial x} \end{bmatrix} \begin{bmatrix} n_x \\ n_z \end{bmatrix} = \begin{bmatrix} 0 \\ 0 \end{bmatrix} \quad . \tag{2}$$

For rough topography, the boundary conforming grid is used to describe the free surface and suppress the artificial scattered waves (Thompson et al., 1985; Hvid, 1994). It can be achieved by the transformation between curvilinear computational space and Cartesian physical space as shown in Fig. 1.

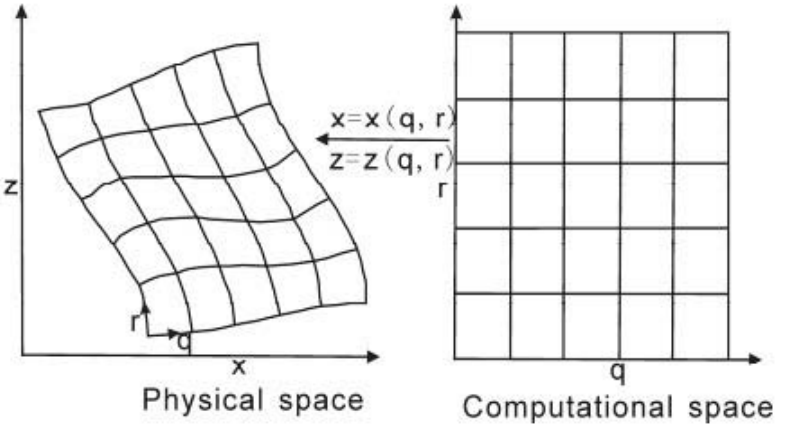

Fig. 1. Mapping between computational space and physical space in two dimensions (Lan and Zhang, 2011).

The relationship between Cartesian coordinates and curvilinear coordinates can be found in Appendix A. Using relationships (A2) - (A3), the wave eqs. (1a) - (1b) can be rewritten in the curvilinear coordinate systems as (Lan et al., 2011)

$$
\begin{aligned}
\rho \frac{\partial^2 \mathrm{u}}{\partial t^2} = \frac{\partial}{\partial q}\Big\{ & q_x \left[c_{11}\left(q_x \partial_q \quad r_x \quad {}_r\right) u \quad c_{13} + \left(q_z \quad {}_q \quad r_z \quad {}_r\right) v \right] \partial \\
& + q_z \left[c_{44}\left(q_x \partial_q \quad r_x \quad {}_r\right) v + c_{44}\left(q_z \quad {}_q \, \partial \, r_z \quad {}_r\right) u \right] \Big\} + \\
& + \frac{\partial}{\partial r}\Big\{ r_x \left[c_{11}\left(q_x \partial_q \quad r_x \quad {}_r\right) u \quad c_{13} + \left(q_z \quad {}_q \quad r_z \quad {}_r\right) v \partial \right] \\
& + r_z \left[c_{44}\left(q_x \partial_q \quad r_x \quad {}_r\right) v + c_{44}\left(q_z \quad {}_q \partial \quad r_z \quad {}_r\right) u \right] \Big\} +
\end{aligned}
\tag{3a}
$$

$$
\begin{aligned}
\rho \frac{\partial^2 \mathrm{v}}{\partial t^2} = \frac{\partial}{\partial q}\Big\{ & q_x \left[c_{44}\left(q_x \partial_q \quad r_x \quad {}_r\right) v \quad c_{44} + \left(q_z \quad {}_q \quad r_z \quad {}_r\right) u \right] \partial \\
& + q_z \left[c_{33}\left(q_z \partial_q \quad r_z \quad {}_r\right) v + c_{13}\left(q_x \quad {}_q \, \partial \, r_x \quad {}_r\right) u \right] \Big\} + \\
& + \frac{\partial}{\partial r}\Big\{ r_x \left[c_{44}\left(q_x \partial_q \quad r_x \quad {}_r\right) v \quad c_{44} + \left(q_z \quad {}_q \quad r_z \quad {}_r\right) u \partial \right] \\
& + r_z \left[c_{33}\left(q_z \partial_q \quad r_z \quad {}_r\right) v + c_{13}\left(q_x \quad {}_q \partial \quad r_x \quad {}_r\right) u \right] \Big\} +
\end{aligned}
\quad . \tag{3b}
$$

Also, using relationships (A-2) - (A-3), the free surface boundary condition (2) can be rewritten in the curvilinear coordinate systems as

$$
\begin{aligned}
& \mathrm{r}_x \left[c_{11}\left(q_x u_q + r_x u_r\right) + c_{13}\left(q_z v_q + r_z v_r\right) \right] \\
& + r_z \left[c_{44}\left(q_z u_q + r_z u_r\right) + c_{44}\left(q_x v_q + r_x v_r\right) \right] = 0
\end{aligned}
\quad , \tag{4a}
$$

$$
\begin{aligned}
& \mathrm{r}_x \left[c_{44}\left(q_x v_q + r_x v_r\right) + c_{44}\left(q_z u_q + r_z u_r\right) \right] \\
& + r_z \left[c_{33}\left(q_z v_q + r_z v_r\right) + c_{13}\left(q_x u_q + r_x u_r\right) \right] = 0
\end{aligned}
\quad . \tag{4b}
$$

Thus, 2D elastic wave equations and irregular free surface have been implemented in the time domain in curvilinear coordinates. In order to add the convolutional perfectly matched layer (CPML) boundary condition to wave eqs. (3a) - (3b), a Fourier transform is used to convert them from the time domain to the frequency domain. Seismic waves are attenuated and decay exponentially when they enter the absorbing layer. Even if the seismic waves reflect from the boundary, after one round trip through the absorbing layer, they have exponentially decayed. Collino and Tsogka (2001) proposed that the CPML can be viewed as an analytical contribution

of the real coordinates in the complex space. Then, the complex coordinates ($\tilde{q}$ and $\tilde{r}$) transformations are (Li and Matar, 2010)

$$\tilde{q} = \int_0^q S_q(q)dq \,, \tag{5a}$$

$$\tilde{r} = \int_0^r S_r(r)dr \,, \tag{5b}$$

where S_q and S_r are the complex frequency shifted (CFS) PML proposed by Kuzuoglu and Mittra (1996). The stretched coordinate metrics are

$$S_{\mathrm{q}} = k_q + \frac{d_q}{\alpha_q + i\omega} \,, \tag{6a}$$

$$S_{\mathrm{r}} = k_r + \frac{d_r}{\alpha_r + i\omega} \,, \tag{6b}$$

where d_q and d_r are attenuation factors along q and r directions; $\alpha_q \geq 0$, $\alpha_r \geq 0$, $k_q \geq 1$ and $k_r \geq 1$. Particularly, we get the classical PML coordinate transformation when $\alpha_q = \alpha_r = 0$ and $k_q = k_r = 1$. In this paper, we take $k_q = k_r = 1$, and $\alpha_{\max} = \pi f_0$ as the maximum value for α_q and α_r which both decrease linearly from the beginning to the end of the CPML layer. f_0 is the dominant frequency of the source.

Using the complex coordinate variables $\tilde{q}$ and $\tilde{r}$ to replace q and r, note that $\partial/\partial\tilde{q} = (1/S_q)\cdot\partial/\partial q$ and $\partial/\partial\tilde{r} = (1/S_r)\cdot\partial/\partial r$. The wave equations in the frequency domain with the CPML boundary condition can be expressed as follows

$$\begin{aligned}
-\omega^2\rho\hat{u} = {} & \frac{1}{S_q}\cdot q_x\cdot\frac{\partial}{\partial \mathrm{q}}\left[c_{11}\left(\frac{1}{S_q}\mathrm{q}_x\partial_q + \frac{1}{S_r}r_x\partial_r\right)\hat{u} + c_{13}\left(\frac{1}{S_q}\mathrm{q}_z\partial_q + \frac{1}{S_r}r_z\partial_r\right)\hat{v}\right] \\
& + \frac{1}{S_q}\cdot q_z\cdot\frac{\partial}{\partial q}\left[c_{44}\left(\frac{1}{S_q}\mathrm{q}_x\partial_q + \frac{1}{S_r}r_x\partial_r\right)\hat{v} + c_{44}\left(\frac{1}{S_q}\mathrm{q}_z\partial_q + \frac{1}{S_r}r_z\partial_r\right)\hat{u}\right] \\
& + \frac{1}{S_r}\cdot r_x\cdot\frac{\partial}{\partial \mathrm{r}}\left[c_{11}\left(\frac{1}{S_q}\mathrm{q}_x\partial_q + \frac{1}{S_r}r_x\partial_r\right)\hat{u} + c_{13}\left(\frac{1}{S_q}\mathrm{q}_z\partial_q + \frac{1}{S_r}r_z\partial_r\right)\hat{v}\right] \\
& + \frac{1}{S_r}\cdot r_z\cdot\frac{\partial}{\partial r}\left[c_{44}\left(\frac{1}{S_q}\mathrm{q}_x\partial_q + \frac{1}{S_r}r_x\partial_r\right)\hat{v} + c_{44}\left(\frac{1}{S_q}\mathrm{q}_z\partial_q + \frac{1}{S_r}r_z\partial_r\right)\hat{u}\right]
\end{aligned} \,, \tag{7a}$$

$$
\begin{aligned}
-\omega^2\rho\hat{\mathrm{v}} = {} & \frac{1}{S_q}\cdot q_x\cdot\frac{\partial}{\partial \mathrm{q}}\left[c_{44}\left(\frac{1}{S_q}\mathrm{q}_x\partial_q+\frac{1}{S_r}r_x\partial_r\right)\hat{v}+c_{44}\left(\frac{1}{S_q}\mathrm{q}_z\partial_q+\frac{1}{S_r}r_z\partial_r\right)\hat{u}\right] \\
& +\frac{1}{S_q}\cdot q_z\cdot\frac{\partial}{\partial q}\left[c_{33}\left(\frac{1}{S_q}\mathrm{q}_z\partial_q+\frac{1}{S_r}r_z\partial_r\right)\hat{v}+c_{13}\left(\frac{1}{S_q}\mathrm{q}_x\partial_q+\frac{1}{S_r}r_x\partial_r\right)\hat{u}\right] \\
& +\frac{1}{S_r}\cdot r_x\cdot\frac{\partial}{\partial \mathrm{r}}\left[c_{44}\left(\frac{1}{S_q}\mathrm{q}_x\partial_q+\frac{1}{S_r}r_x\partial_r\right)\hat{v}+c_{44}\left(\frac{1}{S_q}\mathrm{q}_z\partial_q+\frac{1}{S_r}r_z\partial_r\right)\hat{u}\right] \\
& +\frac{1}{S_r}\cdot r_z\cdot\frac{\partial}{\partial r}\left[c_{33}\left(\frac{1}{S_q}\mathrm{q}_z\partial_q+\frac{1}{S_r}r_z\partial_r\right)\hat{v}+c_{13}\left(\frac{1}{S_q}\mathrm{q}_x\partial_q+\frac{1}{S_r}r_x\partial_r\right)\hat{u}\right]
\end{aligned}
\quad . \qquad (7b)
$$

The expressions (7a) - (7b) are further split into 8 terms and the wave equations are converted back to the time domain by taking an inverse Fourier transform. The equations are shown in Appendix B. In the time domain, these convolution operators from the inverse Fourier transform in eqs. (B-3) - (B-10) are hard to calculate. Matar et al. (2005) proposed memory variables to replace those difficult convolutions. Memory variables are given by (Kuzouglu and Mittra, 1996)

$$\varphi_{i,j}{}^{n} = b_i\cdot\varphi_{i,j}{}^{n-1} + a_i(u_j)^n \quad , \qquad (8a)$$

$$\varphi_{i,j}{}^{n} = b_i\cdot\varphi_{i,j}{}^{n-1} + a_i(v_j)^n \quad , \qquad (8b)$$

where i and j represent the number of grid points in the horizontal and vertical directions, $\varphi_{i,j}$ are memory variables, a_i and b_i are parameters used in memory variables. We use memory variables for elastic wave equations (B3) - (B10) to eliminate convolutions. Then the equations can be rewritten as

$$
u_1 = q_x\cdot\begin{bmatrix} c_{11}\mathrm{q}_x\left(\frac{1}{k_q}\frac{\partial u_q}{\partial q}+\varphi_{q,u_q}\right)+c_{11}\mathrm{r}_x\left(\frac{1}{k_q}\frac{\partial u_r}{\partial q}+\varphi_{\mathrm{q},u_r}\right) \\ +c_{13}\mathrm{q}_z\left(\frac{1}{k_q}\frac{\partial v_q}{\partial q}+\varphi_{q,v_q}\right)+c_{13}\mathrm{r}_z\left(\frac{1}{k_q}\frac{\partial v_r}{\partial q}+\varphi_{\mathrm{q},v_r}\right)\end{bmatrix} \quad , \qquad (9a)
$$

$$
u_2 = q_z\cdot\begin{bmatrix} c_{44}\mathrm{q}_x\left(\frac{1}{k_q}\frac{\partial v_q}{\partial q}+\varphi_{q,v_q}\right)+c_{44}\mathrm{r}_x\left(\frac{1}{k_q}\frac{\partial v_r}{\partial q}+\varphi_{\mathrm{q},v_r}\right) \\ +c_{44}\mathrm{q}_z\left(\frac{1}{k_q}\frac{\partial u_q}{\partial q}+\varphi_{q,u_q}\right)+c_{44}\mathrm{r}_z\left(\frac{1}{k_q}\frac{\partial u_r}{\partial q}+\varphi_{\mathrm{q},u_r}\right)\end{bmatrix} \quad , \qquad (9b)
$$

$$u_3 = r_x \cdot \begin{bmatrix} c_{11}\mathrm{q}_x\left(\frac{1}{k_r}\frac{\partial u_q}{\partial r} + \varphi_{q,u_q}\right) + c_{11}\mathrm{r}_x\left(\frac{1}{k_r}\frac{\partial u_r}{\partial r} + \varphi_{\mathrm{q},u_r}\right) \\ + c_{13}\mathrm{q}_z\left(\frac{1}{k_r}\frac{\partial v_q}{\partial r} + \varphi_{q,v_q}\right) + c_{13}\mathrm{r}_z\left(\frac{1}{k_r}\frac{\partial v_r}{\partial r} + \varphi_{\mathrm{q},v_r}\right) \end{bmatrix}, \quad (9c)$$

$$u_2 = r_z \cdot \begin{bmatrix} c_{44}\mathrm{q}_x\left(\frac{1}{k_r}\frac{\partial v_q}{\partial r} + \varphi_{q,v_q}\right) + c_{44}\mathrm{r}_x\left(\frac{1}{k_r}\frac{\partial v_r}{\partial r} + \varphi_{\mathrm{q},v_r}\right) \\ + c_{44}\mathrm{q}_z\left(\frac{1}{k_r}\frac{\partial u_q}{\partial r} + \varphi_{q,u_q}\right) + c_{44}\mathrm{r}_z\left(\frac{1}{k_r}\frac{\partial u_r}{\partial r} + \varphi_{\mathrm{q},u_r}\right) \end{bmatrix}, \quad (9d)$$

where $\rho\frac{\partial^2 u}{\partial t^2} = u_1 + u_2 + u_3 + u_4$;

$$v_1 = q_x \cdot \begin{bmatrix} c_{44}\mathrm{q}_x\left(\frac{1}{k_q}\frac{\partial v_q}{\partial q} + \varphi_{q,v_q}\right) + c_{44}\mathrm{r}_x\left(\frac{1}{k_q}\frac{\partial v_r}{\partial q} + \varphi_{\mathrm{q},v_r}\right) \\ + c_{44}\mathrm{q}_z\left(\frac{1}{k_q}\frac{\partial u_q}{\partial q} + \varphi_{q,u_q}\right) + c_{44}\mathrm{r}_z\left(\frac{1}{k_q}\frac{\partial u_r}{\partial q} + \varphi_{\mathrm{q},u_r}\right) \end{bmatrix}, \quad (10a)$$

$$v_2 = q_z \cdot \begin{bmatrix} c_{33}\mathrm{q}_z\left(\frac{1}{k_q}\frac{\partial v_q}{\partial q} + \varphi_{q,v_q}\right) + c_{33}\mathrm{r}_z\left(\frac{1}{k_q}\frac{\partial v_r}{\partial q} + \varphi_{\mathrm{q},v_r}\right) \\ + c_{13}\mathrm{q}_x\left(\frac{1}{k_q}\frac{\partial u_q}{\partial q} + \varphi_{q,u_q}\right) + c_{13}\mathrm{r}_x\left(\frac{1}{k_q}\frac{\partial u_r}{\partial q} + \varphi_{\mathrm{q},u_r}\right) \end{bmatrix}, \quad (10b)$$

$$v_3 = r_x \cdot \begin{bmatrix} c_{44}\mathrm{q}_x\left(\frac{1}{k_r}\frac{\partial v_q}{\partial r} + \varphi_{q,v_q}\right) + c_{44}\mathrm{r}_x\left(\frac{1}{k_r}\frac{\partial v_r}{\partial r} + \varphi_{\mathrm{q},v_r}\right) \\ + c_{44}\mathrm{q}_z\left(\frac{1}{k_r}\frac{\partial u_q}{\partial r} + \varphi_{q,u_q}\right) + c_{44}\mathrm{r}_z\left(\frac{1}{k_r}\frac{\partial u_r}{\partial r} + \varphi_{\mathrm{q},u_r}\right) \end{bmatrix}, \quad (10c)$$

$$v_4 = r_z \cdot \begin{bmatrix} c_{33}\mathrm{q}_z\left(\frac{1}{k_r}\frac{\partial v_q}{\partial r} + \varphi_{q,v_q}\right) + c_{33}\mathrm{r}_z\left(\frac{1}{k_r}\frac{\partial v_r}{\partial r} + \varphi_{\mathrm{q},v_r}\right) \\ + c_{13}\mathrm{q}_x\left(\frac{1}{k_r}\frac{\partial u_q}{\partial r} + \varphi_{q,u_q}\right) + c_{13}\mathrm{r}_x\left(\frac{1}{k_r}\frac{\partial u_r}{\partial r} + \varphi_{\mathrm{q},u_r}\right) \end{bmatrix}, \quad (10d)$$

where $\rho\frac{\partial^2 v}{\partial t^2} = v_1 + v_2 + v_3 + v_4$.

The first order derivatives u_q, u_r, v_q and v_r in eqs. (9a) - (9d) are given by

$$\mathrm{u}_q = \frac{1}{k_q}\frac{\partial u}{\partial q} + \varphi_q \quad , \tag{11a}$$

$$\mathrm{u}_r = \frac{1}{k_r}\frac{\partial u}{\partial r} + \varphi_r \quad , \tag{11b}$$

$$\mathrm{v}_q = \frac{1}{k_q}\frac{\partial v}{\partial q} + \varphi_q \quad , \tag{11c}$$

$$\mathrm{v}_r = \frac{1}{k_r}\frac{\partial v}{\partial r} + \varphi_r \quad . \tag{11d}$$

The eqs. (9a) - (10d) are the wave equations applied in curvilinear coordinates with a CPML boundary condition. At the free surface, we use the irregular free surface boundary condition (4a) - (4b) to solve the wave eqs. (9a) - (10d). In the stretched-coordinate metrics, the parameters of the CPML in the q and r directions are shown in Appendix C (Komatitsch and Martin, 2007).

In this study, we use finite-difference methods to approximate elastic wave equations. The forward difference is used at the surface and left boundaries of the model, whereas backward difference is used at the bottom and right boundaries. The central difference is used in the main computing domain of the model (Lan and Zhang, 2011).

GPU IMPLEMENTATION

The Graphic Processing Unit (GPU) was first designed by NVIDIA® to fulfill the growing needs for better computational efficiency in 1999. AMD introduced its first GPU Radeon 256 in 2000. Some studies have shown that utilizing Compute Unified Device Architecture (CUDA) programming language makes it easier to program on NVIDIA® graphics cards (Zhang et al., 2009; Holt and Ernst, 2011). In CUDA parallel programming, the basic computational unit is a thread processor, and thread processors are grouped into multiprocessors. Open CL is comparable with CUDA and is an open programming standard capable of programming Intel, AMD and NVIDIA® GPUs. Since we only have one GPU donated by NVIDIA®, CUDA is used in this research. As GPUs have many thread processors, many threads can execute each kernel at the same time. Each thread has a unique ID that is used to compute memory addresses and make control decisions.

Programming with a GPU, the applications running on hosts and their relevant data should be downloaded to the DRAM (Dynamic Random Access Memory) of the GPU. There is no doubt that the GPU clusters have

better performance than a single GPU. The most time-consuming procedure in parallel computing with multiple GPUs is the communication between GPU and CPU and between different GPUs. For the communication between multiple GPUs, the data is downloaded from one GPU to the host via PCIe Switch and then uploaded to another GPU via PCIe switch. The bottleneck of the communication is the memory bandwidth. As our algorithm is only tested in a relatively small model, there is no need to use a GPU cluster. In the future we will extend our algorithm to larger scales and also a 3D case and will probably use GPU clusters.

The basic execution of a CUDA program runs as follows. For parallel computing, the terminology can be divided into the host, which consists of the CPU and its memory, and the device, which consists of the GPU and its memory. The parallel computing code splits the source file into host related code, which interfaces to the GPU and device components and data-parallel portions of an algorithm which are executed on the device as kernels, only one of which is executed at a time. Each kernel is executed by many threads. CUDA threads are similar to data-parallel tasks in concept. Each thread executes independently and performs the same operations on a subset of a data structure. One CUDA GPU is made of thousands of parallel cores. The first step is to copy input data from CPU memory to GPU DRAM memory. After that, load the GPU program and execute, caching data on the chip for higher performance. The last step is to copy results from GPU memory to CPU memory.

In this study, with free surface boundary condition and the CPML absorbing boundary condition, we use CUDA to simulate wavefield propagation in elastic media with surface topography on a GPU card (NVIDIA® Tesla C2075). The comparison of GPU and CPU parameters are shown in Table 1. We use the CPU to set up the device, allocate data arrays, read input data, generate compute grids and initialize various parameters (e.g., elastic parameters, CPML coefficients and source). Then all of the data are transferred from the CPU to the GPU where the seismic wavefields are calculated at each model grid. Finally, we transfer all of the results back to the CPU and output the files.

Table 1. The device specifications of the CPU and GPU.

	Processing Cores	Clock Frequency (*GHz*)	Memory Bandwidth (*Gb/s*)	Peak Tflops (single)	Total Memory (*Gb*)
CPU: Intel Xeon X5675	6	3.06	32	58.25	24
GPU: Tesla C2075	448	1.15	144	1054.72	6

NUMERICAL EXPERIMENT

In order to illustrate the validity of our numerical algorithms with both a free surface boundary condition and the CPML absorbing boundary condition, seismic wave propagations are simulated in elastic isotropic and anisotropic media. As introduced in Martin et al. (2008), we choose 2D elastic elongated models to test the CPML absorbing performance. For each experiment, the computing codes (conventional CPU version and GPU version) run on the same Dell Precision T7500 64 bit Dual Processor workstation.

The validity of our algorithm is tested with analytical solutions first shown in Aki and Richards (2002). The size of the model is 4.40×1.90 km, the source is located at grid point (220, -95) and two receivers are located at gird points (25, -165) and (405, -25). The density is 2000 kg/m^3, V_P = 3000 m/s and V_S = 2000 m/s. Fig. 2 shows horizontal (x) and vertical (z) components of the displacement recorded by two receivers. Cross correlations of the analytical and numerical results are calculated and shown on each figure panel (Figs. 2a to 2d). Those values of cross correlations are greater than 0.9870 which proves the correctness of our algorithm.

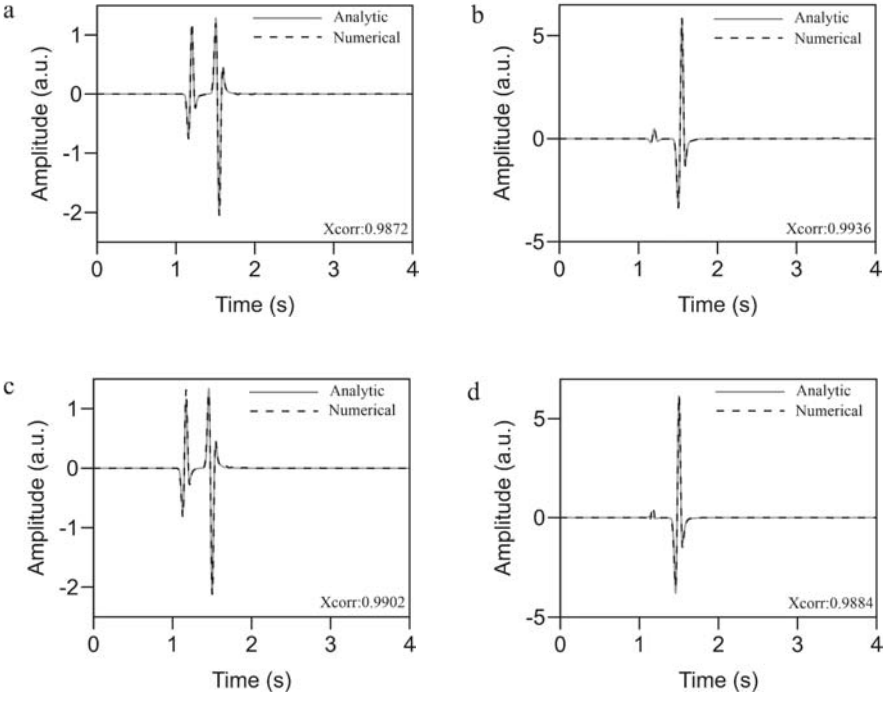

Fig. 2. Horizontal (x) and vertical (z) components of the displacement recorded by the receivers R1 (25, -165) (a and b) and R2 (405, -25) (c and d) by using an analytical solution and our algorithm. Grey solid lines: seismograms of analytical solution; black dashed lines: seismograms calculated with our algorithm. Xcorr: cross correlation.

Numerical modeling in the 2D isotropic elongated model

For the isotropic medium ($c_{11} = c_{33}$), the density is 2000 kg/m^3, V_P = 3000 m/s and V_S = 2000 m/s, so the elastic parameters are $c_{11} = 18 \times 10^9$ (Pa), $c_{13} = 2 \times 10^9$ (Pa), $c_{33} = 18 \times 10^9$ (Pa) and $c_{44} = 8 \times 10^9$ (Pa), respectively. The topography of this model is denoted by a shape of a wide hill. The size of the model is 4.30 × 1.65 km, and it is discretized using a grid comprised of 430 ×165 grid points with a grid point spacing of 10 m (Fig. 3). The thickness of the CPML boundary is 150 m (15 grid points). We focus more on the shallow formations to study the effect of the free surface on wave propagation.

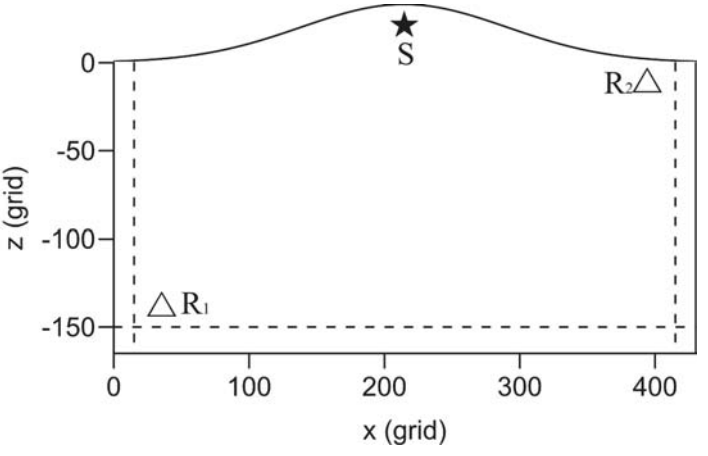

Fig. 3. The model with a shape of a hill. The star denotes the source S. The triangles denote receivers R_1 and R_2. The dashed lines represent the CPML boundaries.

The Ricker wavelet is used as a function of vertical point source in these numerical experiments, which is given by

$$f(t) = \left(1 - 2\left(\pi \cdot f_0\left(t - 0.5\right)\right)^2\right) e^{-\left(\pi \cdot f_0 (t-0.5)\right)^2} \quad , \tag{15}$$

where the peak frequency f_0 = 10 Hz. The sampling rate is 1 ms. In order to avoid dispersion in seismic numerical modeling, the stability relationship is considered by calculating $\lambda_s = V_s T = V_s / f = 2000\ m/s / 10\ Hz = 200\, m$. That means there are 20 grid points per minimum wavelength which is more than enough to guarantee the stability of the numerical method.

The source is located at grid position (215, 10). Two receivers are located at grid positions (25, 140) and (405, 10), which are very close to the inner side of the CPML boundary (10 grid points). This makes it easier to observe the artificial reflections if CPML does not work well. In the model with irregular surface (Fig. 3), the source S, geophones R_1 and R_2 and CPML boundaries are marked as a star, the triangles and dashed lines, respectively.

Fig. 4 shows the snapshots of the displacement in the vertical plane at 0.8 s, 1.2 s and 4.0 s, respectively. The snapshots (a, b, c) in the left column and the snapshots (d, e, f) in the right column are generated by numerical wavefield simulations with CPML and PML boundary conditions, respectively. One can clearly observe not only seismic P- and S-waves, but also Rayleigh waves (R) and Head waves (H). Figs. 3e and 3f show the distinct artificial reflections generated by numerical modeling with PML, which means CPML works much better than PML to absorb unwanted seismic reflections at the edges of the model with surface topography.

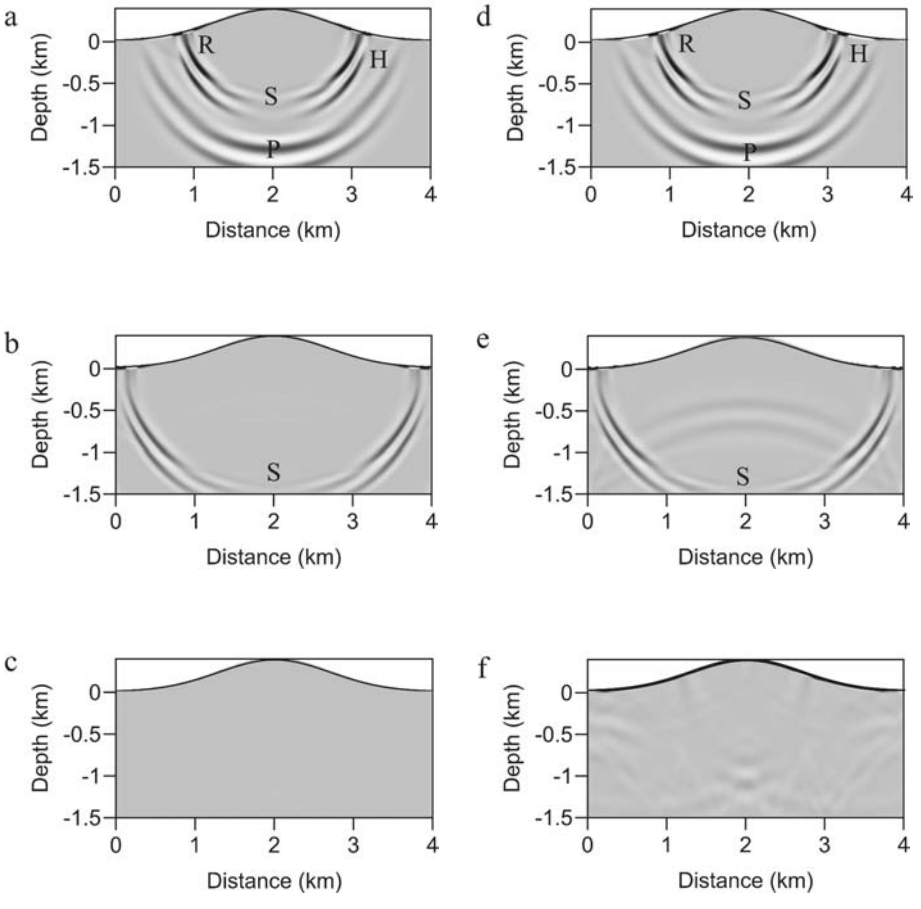

Fig. 4. Snapshots of the displacement in the vertical plane at 0.8 s, 1.2 s and 4.0 s in an isotropic medium. P: Compressional wave; S: Shear wave; R: Rayleigh wave; H: Head wave. Wavefield simulation with CPML (a to c); wavefield simulation with PML (d to f).

Fig. 5 shows the horizontal (x) and vertical (z) components of the displacement recorded by the receivers R_1 (a and b) and R_2 (c and d). To

check the validity of our numerical algorithms, a large model (grids comprised of 1230×915) is chosen to represent unbounded media. One can find that the seismograms obtained by numerical modeling with CPML (dark dotted lines) have great agreement with the seismograms (grey solid lines) obtained from the large model. However, severe artificial reflections are found in the seismograms obtained by numerical modeling with PML (dark dashed lines).

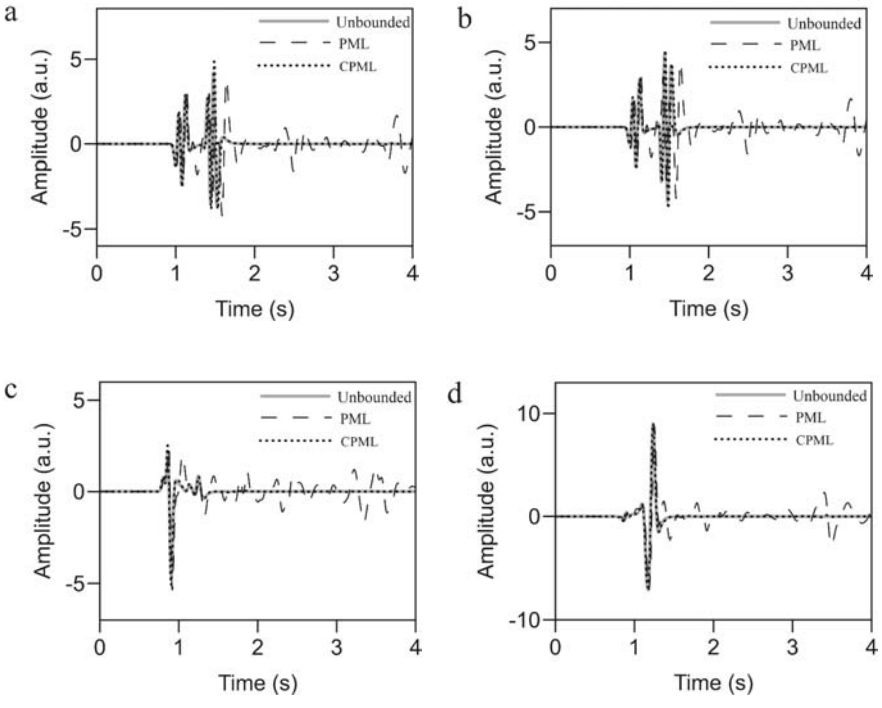

Fig. 5. Horizontal (x) and vertical (z) components of the displacement recorded by the receivers R_1 (a and b) and R_2 (c and d) in an isotropic medium. Grey solid lines: seismograms calculated in unbounded medium; dark dotted lines: seismograms calculated with CPML boundary condition; dark dashed lines: seismograms calculated with PML boundary condition.

For simplicity, we take the square of wave amplitude as the energy of seismic wave propagation. Fig. 6 shows wavefield energy decay curves calculated from wavefield simulations with CPML and PML boundary conditions in isotropic media. The energy is absorbed gradually after 0.76 s, which is the time that the outgoing seismic P-wave first reaches the inner side of the absorbing layers. Theoretically, there is no energy remaining in the medium after 1.17 s, because P-, S- and Rayleigh waves have left the main computational domain. After 1.17 s, one can observe that the energy calculated by numerical modeling with CPML reduces faster than that calculated by PML, which means CPML has a better absorbing ability than PML.

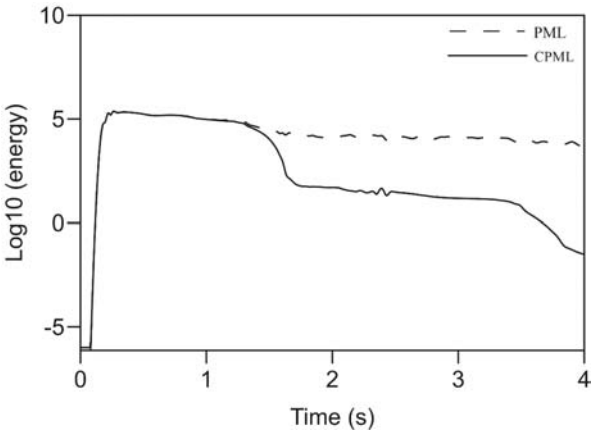

Fig. 6. Wavefield energy decay curves calculated with CPML and PML boundary conditions in an isotropic medium.

Numerical modeling in the anisotropic elongated model

In this model, the density is $3000\ kg/m^3$ and the elastic parameters are $c_{11} = 4\times10^9\,(Pa)$, $c_{13} = 3.8\times10^9\,(Pa)$, $c_{33} = 20\times10^9\,(Pa)$, and $c_{44} = 2\times10^9\,(Pa)$, respectively (Li and Matar, 2010). The positions of the source and receivers are exactly the same as those used in the previous study (Fig. 2). The dominant source frequency is 5 Hz.

Fig. 7 shows the snapshots of the displacement in the vertical plane at 1.2 s, 2.0 s, 2.8 s and 6.0 s, respectively. The snapshots (a, b, c, d) in the left column and snapshots (e, f, g, h) in the right column are generated by wavefield simulations with CPML and PML boundary conditions, respectively. We can clearly observe all the seismic wave phases (quasi-P, quasi-S, Rayleigh and Head waves). The distinct artificial reflections can be seen in the numerical modeling with PML (Figs. 7e-7h in the right column), which means CPML also works better than PML to absorb outgoing seismic waves at the edges of the anisotropic model with rough topography. Because PML does not work very well to absorb P-waves, some artifacts in the center upper part of Figs. 7f and 7g are observed. These are the P-wave reflections from bottom boundaries and the irregular free surface.

Fig. 8 shows the horizontal (x) and vertical (z) components of the displacement recorded by the receivers R_1 (a and b) and R_2 (c and d). The seismograms obtained by numerical modeling with CPML (dark dotted lines) match the seismograms (grey solid lines) obtained from the large model. However, severe artificial reflections are found from the seismograms generated by numerical modeling with PML (dark dashed lines). Because of the close proximity (10 grid points) between receivers and the inner side of the boundary, the outgoing quasi-S-waves are seriously distorted by the artificial reflections of quasi-P-waves.

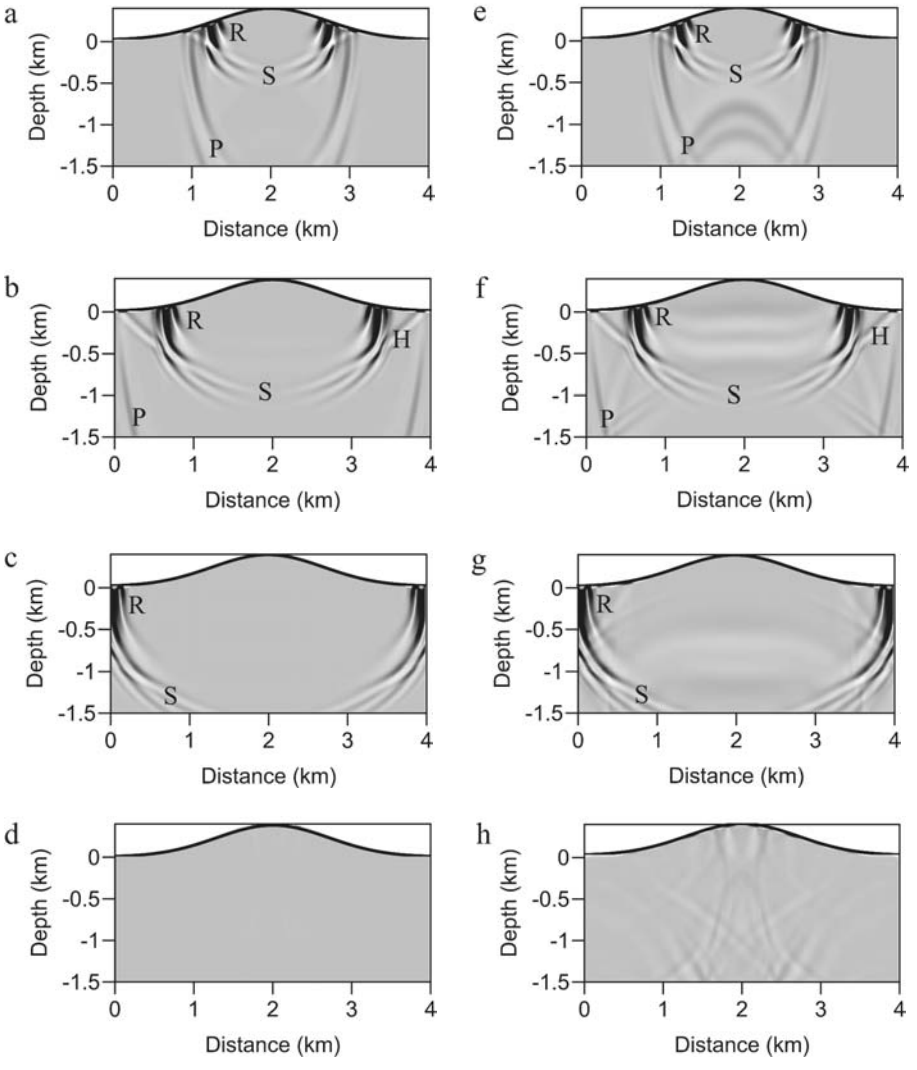

Fig. 7. Snapshots of the displacement in the vertical plane at 1.2 s, 2.0 s, 2.8 s and 6.0 s in an anisotropic medium. P: Compressional wave; S: Shear wave; R: Rayleigh wave; H: Head wave. Wavefield simulation with CPML (a to d); wavefield simulation with PML (e to h).

Fig. 9 shows wavefield energy decay curves calculated from wavefield simulations with CPML and PML boundary conditions in an anisotropic medium. The CPML and PML start absorbing the energy gradually after the outgoing quasi-P wave first reaches the inner edge of the absorbing layers (1.82 s). After 2.44 s, theoretically, there is no energy remaining in the medium, because all seismic wave phases have left the main computational domain. We find that the energy calculated by numerical modeling with CPML abruptly decreases after 2.44 s, and the

energy absorption of CPML is faster than that of PML, which means CPML works better than PML in absorbing outgoing seismic waves.

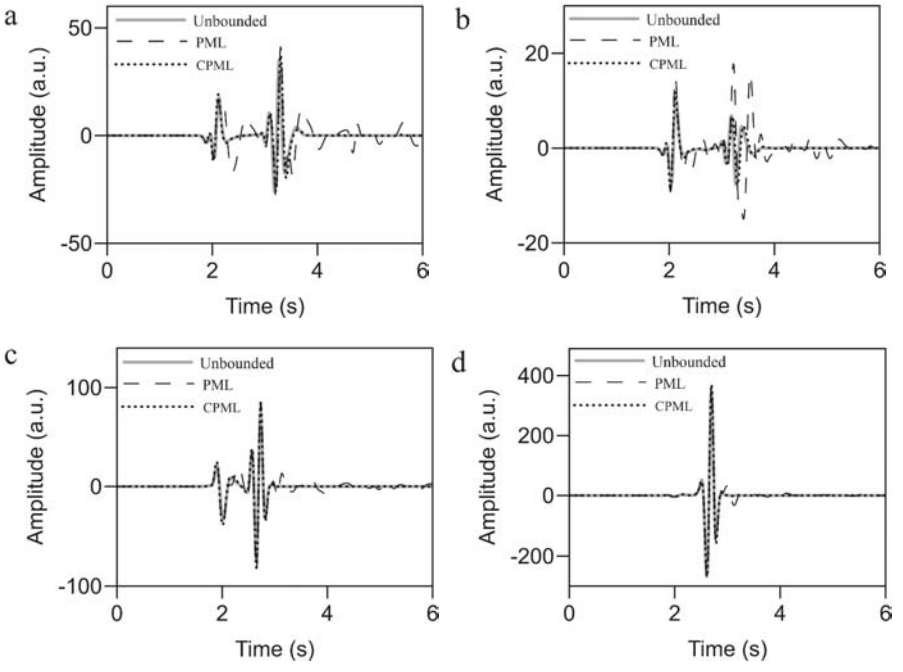

Fig. 8. Horizontal (x) and vertical (z) components of the displacement recorded by the receivers R_1 (a and b) and R_2 (c and d) in an anisotropic medium. Grey solid lines: seismograms calculated in unbounded medium; dark dotted lines: seismograms calculated with CPML boundary condition; dark dashed lines: seismograms calculated with PML boundary condition.

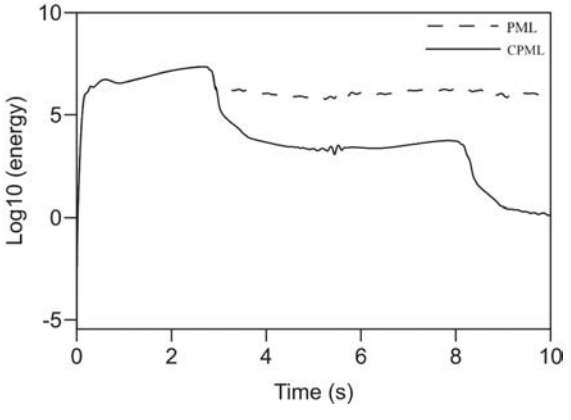

Fig. 9. Wavefield energy decay curves calculated with CPML and PML boundary conditions in an anisotropic medium.

To further test the CPML absorbing performance, we ran seismic wavefield simulations up to 10 s. Fig. 10 shows horizontal (x) and vertical (z) components of the displacement recorded by the receivers R_1 (Figs. 10a and 10b) and R_2 (Figs. 10c and 10d) by using CPML and PML boundary conditions. We found that the numerical modeling with CPML is still stable due to the excellent absorbing ability of CPML. However, the seismic wavefields calculated with PML are seriously contaminated due to the strong artificial reflections.

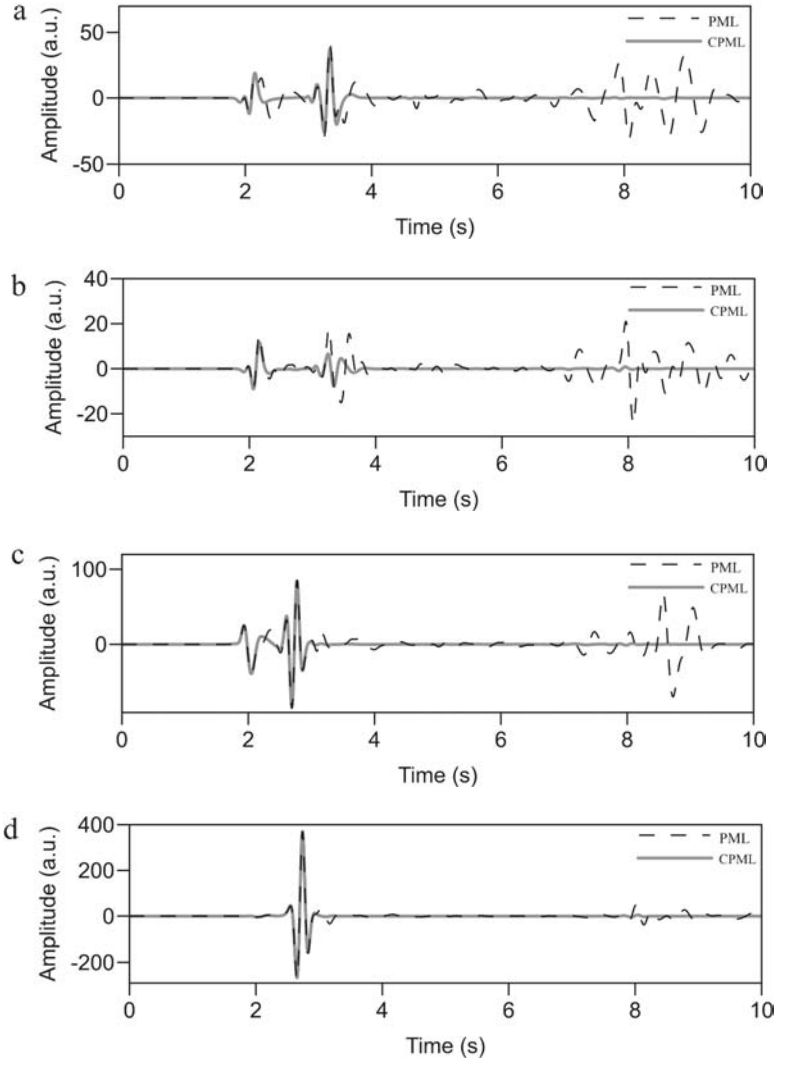

Fig. 10. Horizontal (x) and vertical (z) components of the displacement in long simulation run (10 s) recorded by the receivers R_1 (a and b) and R_2 (c and d) in an anisotropic medium. Grey solid lines: seismograms calculated with CPML boundary condition; dark dashed lines: seismograms calculated with PML boundary condition.

In our study, GPU parallel computing on a NVIDIA® GPU card (Tesla C2075) has been applied to accelerate the numerical simulation of seismic wave propagation in elastic isotropic and anisotropic media with rough topography. Our tests demonstrate that GPU parallel code is running 10 times faster than conventional CPU sequential code on the same workstation (Dell Precision T7500 64bit Dual Processor). All of the CPU cores are used. The computation acceleration of 10 times is reasonable considering our hardware, model parameters and model size. What is more, the factor that restricts more acceleration is the communication between CPU and GPU memory.

Numerical modeling in the non-symmetric free surface model

A non-symmetric model with two hills is built to further test the validity of our algorithm. The density is $2000\ kg/m^3$, $V_P = 3000\ m/s$ and $V_S = 2000\ m/s$, so the elastic parameters are $c_{11} = 18\times10^9\ (Pa)$, $c_{13} = 2\times10^9\ (Pa)$, $c_{33} = 18\times10^9\ (Pa)$ and $c_{44} = 8\times10^9\ (Pa)$, respectively. The size of the model is 4.40 *km* × 1.70 *km*, and it is discretized using a grid comprised of 440×170 grid points with a grid point spacing of 10 m (Fig. 11). The thickness of the CPML boundary is 200 m (20 grid points). The source is located at grid position (220, 10).

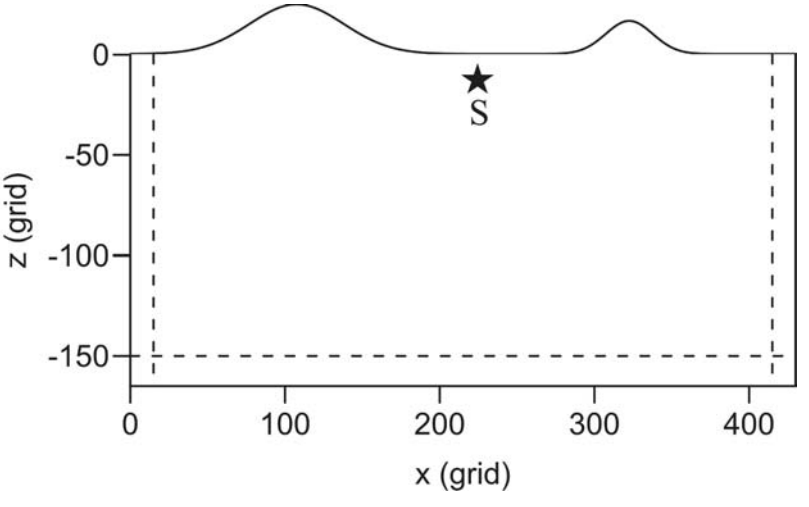

Fig. 11. The model with a shape of two hills. The star denotes the source S. The dashed lines represent the CPML boundaries.

Fig. 12 shows the snapshots of the displacement in the vertical plane at 0.8 s, 1.2 s, 1.6 s and 4.0 s, respectively. It shows clearly not only seismic P, S, Rayleigh (R) and Head (H) waves, but also Rayleigh wave scatters to P-wave (RP) and S-wave (RS).

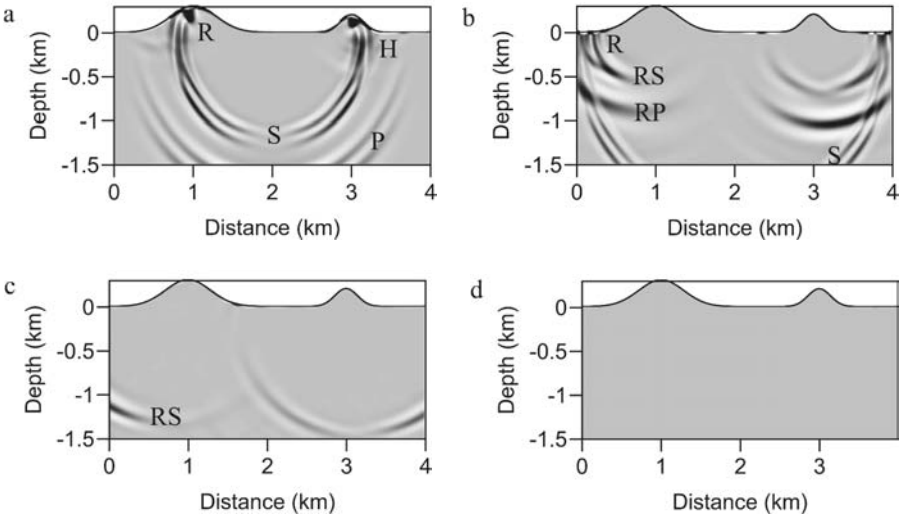

Fig. 12. Snapshots of the displacement in the vertical plane at 0.8 s, 1.2 s, 1.6 s and 4.0 s in an isotropic medium. P: Compressional wave; S: Shear wave; R: Rayleigh wave; H: Head wave. RP: Rayleigh wave scatters to P-wave; RS: Rayleigh wave scatters to S-wave.

Fig. 13 shows the synthetic seismic profiles of the horizontal components (a) and vertical components (b) of the displacement. We can observe P-wave, R-wave, P-wave diffracts to P-wave (PdP), Rayleigh wave reflections to Rayleigh wave (RR), Rayleigh wave diffractions to Rayleigh wave (RdR), and Rayleigh wave scatters to P-wave which propagate both backward (RPb) and forward (RPf). The RR wave and RS wave are hard to separate in the seismic profiles because the velocities of S- and Rayleigh waves are very close. In addition, the reflections and scatter waves of the right hill have higher energy because the right hill is smaller and steeper than the left one.

DISCUSSION

Our algorithm basically obeys the rule that there should be at least ten grid points per shear wavelength. In addition, the stability condition $c_s \Delta t \le \Delta h / \sqrt{2}$ is used in our algorithm. The numerical test presented in the paper is just an example; our algorithm is also suitable for higher frequencies. However, dispersion and exponential blow up phenomena were observed in seismic numerical modeling in anisotropic media with classic PML absorbing boundary condition (Collino and Tsogka, 2001; Bécache et al., 2003). Even for CPML, it is also intrinsically unstable. This is because PML or CPML both generate spurious modes traveling and growing along the absorbing layers when waves impinge the boundary at grazing incidence (Komatitsch and Martin, 2007; Martin and Komatitsch, 2009). In free surface modeling with Rayleigh waves, the instability of PML and CPML is

strongly related to the wave phenomena, especially when the Poisson's ratio of the medium is high (Zeng et al., 2011).

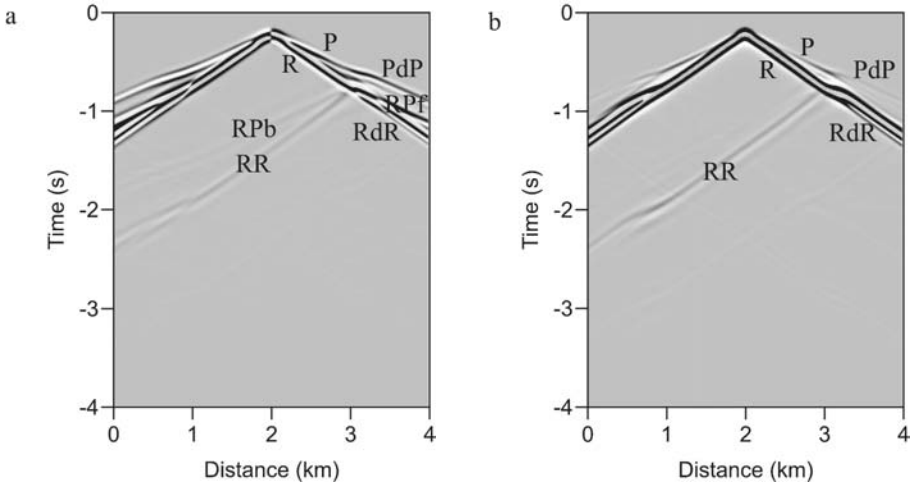

Fig. 13. Synthetic seismic profiles of the horizontal components (a) and vertical components (b) of the displacement. P: direct quasi-compressional wave; R: direct Rayleigh wave; RR: Rayleigh wave reflections to Rayleigh wave; RdR: Rayleigh wave diffractions to Rayleigh wave; RPb: Rayleigh wave scatters to P-wave and propagates backward; RPf: Rayleigh wave scatters to P-wave and propagates forward; PdP: P-wave diffracts to P-wave.

Although it does not show up in this paper, we have noticed that the stability of CPML with an irregular free surface is related to the selection of anisotropic parameters. Meza-Fajardo and Papageorgiou (2008) presented Multi-axial PML (MPML) in seismic modeling, which leads to better numerical stability in anisotropic elastic wave propagation. So, in the future, additional stability analysis is needed for anisotropic media with an irregular surface topography using a suitable boundary condition.

CONCLUSIONS

We incorporated the convolutional perfectly matched layer (CPML) boundary condition into wave equations in the curvilinear coordinate system. Both a free surface boundary condition and the CPML absorbing boundary condition were used in the implementation of the numerical algorithm in elastic isotropic and anisotropic media with rough topography in curvilinear coordinates. Numerical examples show that our algorithm can accurately simulate seismic wave propagation, and CPML is more effective in suppressing artificial reflections than perfectly matched layer (PML). Additionally, GPU parallel computing on an NVIDIA® GPU card greatly accelerates the numerical simulation of seismic wave propagation (10 times faster than conventional CPU code). Seismic numerical modeling with a

more stable boundary condition (e.g. multi-axial PML) will be investigated in a follow-up study.

ACKNOWLEDGEMENTS

The authors acknowledge the Faculty Internationalization Grant at The University of Tulsa. We thank NVIDIA® Corporation for the donation of a GPU (Graphic Processing Unit) card, Tesla C2075. The authors also thank Keith Willson, Dr. Tao Zhao and Professor Brenton McLaury at The University of Tulsa for their help. We appreciate an anonymous reviewer for the valuable suggestions on improving the quality of this paper.

REFERENCES

Abarbanel, S., Gottlieb, D. and Hesthaven, J.S., 1999. Well-posed perfectly matched layers for advective acoustics. J. Computat. Phys., 154: 266-283.

Abdelkhalek, R., Calendra, H., Coulaud, O., Latu, G. and Roman, J., 2009. Fast seismic modeling and reverse time migration on a GPU cluster. The 2009 High Perform. Comput. Simulat., 6: 36-43.

Aki, K. and Richards, P.G., 2002. Quantitative Seismology. 2nd ed., University Science Books, Sausalito.

Alterman, Z. and Karal, F.C., 1968. Propagation of elastic waves in layered media by finite difference methods. Bull. Seismol. Soc. Am., 58: 367-398.

Appelö, D. and Peterson, N.A., 2009. A stable finite difference method for the elastic wave equation on complex geometries with free surfaces. Commun. Computat. Phys., 5: 84-107.

Bécache, E., Fauqueux, S. and Joly, P., 2003. Stability of perfectly matched layers, group velocities and anisotropic waves. J. Computat. Phys., 188: 399-433.

Bérenger, J.P., 1994. A perfectly matched layer for the absorption of electromagnetic waves. J. Computat. Phys., 114: 185-200.

Cerjan, C., Kosloff, D., Kosloff, R. and Reshef, M., 1985. A nonreflecting boundary condition for discrete acoustic and elastic wave equations. Geophysics, 50: 705-708.

Chen, J., Bording, P., Liu, E., Zhang, Z. and Badal, J., 2010. The application of the nearly optimal sponge boundary conditions for seismic wave propagation in poroelastic media. J. Seismic Explor., 19: 1-19.

Collino, F. and Tsogka, C., 2001. Application of the perfectly matched absorbing layer model to the linear elastodynamic problem in anisotropic heterogeneous media. Geophysics, 66: 294-307.

Drossaert F.H. and Giannopoulos, A., 2007. Complex frequency shifted convolution PML for FDTD modeling of elastic waves. Wave Motion, 44: 593-604.

Galis, M., Moczo, P. and Kristek, J., 2008. A 3-D hybrid finite-difference - finite-element viscoelastic modelling of seismic wave motion. Geophys. J. Internat., 175: 153-184.

Holt, B. and Ernst, D., 2011. Accelerating Geophysics Simulation using CUDA. J. Computat. Sci. Educ., 2: 21-27.

Hvid, S.L., 1994. Three dimensional algebraic grid generation. PhD thesis, Technical University of Denmark, Lyngby.

Ilan, A., Ungar, A. and Alterman, Z.S., 1975. An improved representation of boundary conditions in finite difference schemes for seismological problems. Geophys. J. Roy. Astronom. Soc., 43: 727-745.

Ilan, A., 1978. Stability of finite difference schemes for the problem of elastic wave propagation in a quarter plane. J. Computat. Phys., 29: 389-403.

Komatitsch, D. and Tromp, J., 1999. Introduction to the spectral element method for three-dimensional seismic wave propagation. Geophys. J. Internat., 139: 806-822.

Komatitsch, D. and Tromp, J., 2003. A perfectly matched layer absorbing boundary condition for the second-order seismic wave equation. Geophys. J. Internat., 154: 146-153.

Komatitsch, D. and Martin, R., 2007. An unsplit convolutional perfectly matched layer improved at grazing incidence for the seismic wave equation. Geophysics, 72: 155-167.

Kuzuoglu, M. and Mittra, R., 1996. Frequency dependence of the constitutive parameters of causal perfectly matched anisotropic absorbers. IEEE, 6: 447-449.

Lan, H., Liu, J. and Bai, Z., 2011. Wave-field simulation in VTI media with irregular free surface. Chin. J. Geophys., 54: 2072-2084.

Lan, H. and Zhang, Z., 2011. Three-dimensional wave-field simulation in Heterogeneous transversely isotropic media with irregular free surface. Bull. Seismol. Soc. Am., 101: 1354-1370.

Lan, H., Chen, J., Zhang, Z., Liu, Y., Zhao, J. and Shi, R., 2016. Application of the perfectly matched layer in seismic wavefield simulation with an irregular free surface. Geophys. Prosp., 64: 112-128. doi: 10.1111/1365-2478.12260.

Li, Y. and Matar, O.B., 2010. Convolutional perfectly matched layer for elastic second-order wave equation. J. Acoust. Soc. Am., 127: 1318-1327.

Liu, H., Li, B., Liu, H., Tong, X., Liu, Q. and Wang, X., 2012. The issues of pre-stack reverse time migration and solutions with Graphic Processing Unit implementation. Geophys. Prosp., 60: 906-918.

Liu, L., Ding, R., Liu, H. and Liu, H., 2015. 3D hybrid-domain full waveform inversion on GPU. Comput. Geosci., 83: 27-36.

Lisitsa, V., Tcheverda, V. and Botter, C., 2016. Combination of the discontinuous Galerkin method with finite differences for simulation of seismic wave propagation. J. Computat. Phys., 311: 142-157.

Martin, R., Komatischa, D. and Ezziani, A., 2008. An unsplit convolutional perfectly matched layer improved at grazing incidence for the seismic wave equation in poroelastic media. Geophysics, 73; 51-61.

Martin, R. and Komatitsch, D., 2009. An unsplit convolutional perfectly matched layer technique improved at grazing incidence for the viscoelastic wave equation. Geophys. J. Internat., 179: 333-344.

Matar, O.B., Preobrazhensky, V. and Pernod, P., 2005. Two-dimensional axi-symmetric numerical simulation of supercritical phase conjugation of ultrasound in active solid media. J. Acoust. Soc. Am., 118: 2880-2890.

Meza-Fajardo, K. and Papageorgiou A., 2008. A nonconvolutional, split-field, perfectly matched layer for wave propagation in isotropic and anisotropic elastic media: Stability analysis. Bull. Seismol. Soc. Am., 98: 1811–1836.

Michéa, D. and Komatitsch, D., 2010. Accelerating a 3D finite difference wave propagation code using GPU graphic cards. Geophysics Journal International, 182, 389-402.

Micikevicius, P., 2009. 3D finite difference computation on GPUs using CUDA. Proc. 2nd Workshop General Purpose Processing Graphics Processing Units: 79-84.

Nielsen, P., If, F., Berg, P. and Skovgaard, O., 1994. Using the pseudo-spectral technique on curved grids for 2D acoustic forward modeling. Geophys. Prosp., 42: 321-342.

Nilsson, S., Petersson, N.A., Sjogreen, B. and Kreiss, H.O., 2007. Stable difference approximations for the elastic wave equation in second order formulation. SIAM J. Numer. Analys., 45: 1902-1936.

Panetta, J., Teixeira, T., de Souza Filho, P.R., da Cunha Finho, C.A., Sotelo, D., da Motta, F.M.R., Pinheiro, S.S., Junior, I.P., Rosa, A.L.R., Monnerat, L.R. and Carneiro, L.T., 2009. Accelerating Kirchhoff migration by CPU and GPU cooperation. 21st Symp. Computer Architecture and High Performance Computing, Sao Paulo: 26-32.

Preis, T., 2011. GPU-computing in econophysics and statistical physics. European Physical Journal Special Topics, 194: 87-119.

Roden, J.A. and Gedney, S.D., 2000. Convolutional PML(C-PML): An efficient FDTD implementation of the CFS-PML for arbitrary media. Microw. Optic. Technol. Lett., 27: 334-339.

Shin, J., Ha, W., Jun, H., Min, D.J. and Shin, C., 2014. 3D Laplace-domain full waveform inversion using a single GPU card. Comput. Geosci., 67: 1-13.

Sofronov, I., Zaitsev, N. and Dovgilovich, L., 2015. Multi-block finite- difference method for 3D elastodynamic simulations in anisotropic subhorizontally layered media. Geophys. Prosp., 63: 1142-1160.

Tarrass, I., Giraud, L. and Thore, P., 2011. New Curvilinear scheme for elastic wave propagation in presence of curved topography. Geophys. Prosp., 59: 889-906.

Tessmer, E., Kosloff, D. and Behle, A., 1992. Elastic wave propagation simulation in the presence of surface topography. Geophys. J. Internat., 108: 621-632.

Thompson, J.F., Warsi, Z.U.A. and Mastin, C.W., 1985. Numercial Grid Generation Foundations and Applicatioins. North Holland Publishing Company, New York.

Vidale, J. and Clayton, R., 1986. A stable free-surface boundary condition for two-dimensional elastic finite -difference wave simulation. Geophysics, 51: 2247-2249.

Yang, P., Gao, J. and Wang, B., 2015. A graphics processing unit implementation of time-domain full-waveform inversion. Geophysics, 80(3): F31-F39.

Zeng, C., Xia, J., Miller, R.D. and Tsoflias, G.P., 2011. Application of the multiaxial perfectly matched layer (M-PML) to near-surface seismic modeling with Rayleigh waves. Geophysics, 76: 43-52.

Zhang, J.H., Wang, S.Q. and Yao, Z.X., 2009. Accelerating 3D Fourier migration with Graphics Processing Units. Geophysics, 74: 129-139.

APPENDIX A

The grid points (x,z) of the Cartesian coordinates are determined from the grid point $(q,r)$of the curvilinear coordinates with the equation

$$\begin{aligned} x &= x(q,r) \\ z &= z(q,r). \end{aligned} \tag{A-1}$$

Then, spatial derivatives can be achieved in the Cartesian coordinate system from the curvilinear coordinate system following the chain rules (Lan et al., 2011)

$$\partial_{\mathrm{x}} = q_x \partial_q + r_x \partial_r, \tag{A-2}$$

$$\partial_{\mathrm{z}} = q_z \partial_q + r_z \partial_r. \tag{A-3}$$

where q_x, q_z, r_x and r_z denote $\partial_q(x,z)/\partial_x$, $\partial_q(x,z)/\partial_z$, $\partial_r(x,z)/\partial_x$ and $\partial_r(x,z)/\partial_z$, respectively. Similarly, we can express spatial derivatives in the curvilinear coordinate system (q,r)

$$\partial_{\mathrm{q}} = x_q \partial_x + z_q \partial_z, \tag{A-4}$$

$$\partial_{\mathrm{r}} = x_r \partial_x + z_r \partial_z. \tag{A-5}$$

These kinds of derivatives are called metric derivatives (Lan et al., 2011)

$$q_x = \frac{z_r}{J}, q_z = \frac{-x_r}{J}, \tag{A-6}$$

$$r_x = \frac{-z_q}{J}, r_z = \frac{x_q}{J}, \tag{A-7}$$

where z_r, z_q, x_r and x_r denote $\partial_z(q,r)/\partial_r$, $\partial_z(q,r)/\partial_q$, $\partial_x(q,r)/\partial_r$ and $\partial_x(q,r)/\partial_r$, respectively. The Jacobian of the transformation J is given by

$$J = \mathrm{x}_q z_r - x_r z_q. \tag{A-8}$$

APPENDIX B

The expressions (7a) - (7b) are further split into eight terms and the wave equations are converted back to the time domain by taking an inverse Fourier transform leading to the following expressions

$$\rho \frac{\partial^2 u}{\partial t^2} = u_1 + u_2 + u_3 + u_4, \tag{B-1}$$

$$\rho \frac{\partial^2 v}{\partial t^2} = v_1 + v_2 + v_3 + v_4, \tag{B-2}$$

where

$$u_1 = F^{-1}\left(\frac{1}{S_q}\right) \cdot q_x * \frac{\partial}{\partial \mathrm{q}} \begin{bmatrix} c_{11}\left(F^{-1}\left(\frac{1}{S_q}\right)\mathrm{q}_x * \partial_q + F^{-1}\left(\frac{1}{S_r}\right) r_x * \partial_r\right) u \\ + c_{13}\left(F^{-1}\left(\frac{1}{S_q}\right)\mathrm{q}_z * \partial_q + F^{-1}\left(\frac{1}{S_r}\right) r_z * \partial_r\right) v \end{bmatrix}, \tag{B-3}$$

$$u_2 = F^{-1}\left(\frac{1}{S_q}\right) \cdot q_z * \frac{\partial}{\partial q} \begin{bmatrix} c_{44}\left(F^{-1}\left(\frac{1}{S_q}\right)\mathrm{q}_x * \partial_q + F^{-1}\left(\frac{1}{S_r}\right) r_x * \partial_r\right) v \\ + c_{44}\left(F^{-1}\left(\frac{1}{S_q}\right)\mathrm{q}_z * \partial_q + F^{-1}\left(\frac{1}{S_r}\right) r_z * \partial_r\right) u \end{bmatrix}, \tag{B-4}$$

$$u_3 = F^{-1}\left(\frac{1}{S_r}\right) \cdot r_x * \frac{\partial}{\partial \mathrm{r}} \begin{bmatrix} c_{11}\left(F^{-1}\left(\frac{1}{S_q}\right)\mathrm{q}_x * \partial_q + F^{-1}\left(\frac{1}{S_r}\right) r_x * \partial_r\right) u \\ + c_{13}\left(F^{-1}\left(\frac{1}{S_q}\right)\mathrm{q}_z * \partial_q + F^{-1}\left(\frac{1}{S_r}\right) r_z * \partial_r\right) v \end{bmatrix}, \tag{B-5}$$

$$u_4 = F^{-1}\left(\frac{1}{S_r}\right) \cdot r_z * \frac{\partial}{\partial r} \begin{bmatrix} c_{44}\left(F^{-1}\left(\frac{1}{S_q}\right)\mathrm{q}_x * \partial_q + F^{-1}\left(\frac{1}{S_r}\right) r_x * \partial_r\right) v \\ + c_{44}\left(F^{-1}\left(\frac{1}{S_q}\right)\mathrm{q}_z * \partial_q + F^{-1}\left(\frac{1}{S_r}\right) r_z * \partial_r\right) u \end{bmatrix}, \tag{B-6}$$

$$v_1 = F^{-1}\left(\frac{1}{S_q}\right)\cdot q_x * \frac{\partial}{\partial \mathrm{q}}\left[\begin{array}{l} c_{44}\left(F^{-1}\left(\frac{1}{S_q}\right)\mathrm{q}_x * \partial_q + F^{-1}\left(\frac{1}{S_\mathrm{r}}\right)r_x * \partial_r\right)v \\ + c_{44}\left(F^{-1}\left(\frac{1}{S_q}\right)\mathrm{q}_z * \partial_q + F^{-1}\left(\frac{1}{S_\mathrm{r}}\right)r_z * \partial_r\right)u \end{array}\right], \quad \text{(B-7)}$$

$$v_2 = F^{-1}\left(\frac{1}{S_q}\right)\cdot q_z * \frac{\partial}{\partial q}\left[\begin{array}{l} c_{33}\left(F^{-1}\left(\frac{1}{S_q}\right)\mathrm{q}_z * \partial_q + F^{-1}\left(\frac{1}{S_\mathrm{r}}\right)r_z * \partial_r\right)v \\ + c_{13}\left(F^{-1}\left(\frac{1}{S_q}\right)\mathrm{q}_x * \partial_q + F^{-1}\left(\frac{1}{S_\mathrm{r}}\right)r_x * \partial_r\right)u \end{array}\right], \quad \text{(B-8)}$$

$$v_3 = F^{-1}\left(\frac{1}{S_\mathrm{r}}\right)\cdot r_x * \frac{\partial}{\partial \mathrm{r}}\left[\begin{array}{l} c_{44}\left(F^{-1}\left(\frac{1}{S_q}\right)\mathrm{q}_x * \partial_q + F^{-1}\left(\frac{1}{S_\mathrm{r}}\right)r_x * \partial_r\right)v \\ + c_{44}\left(F^{-1}\left(\frac{1}{S_q}\right)\mathrm{q}_z * \partial_q + F^{-1}\left(\frac{1}{S_\mathrm{r}}\right)r_z * \partial_r\right)v \end{array}\right], \quad \text{(B-9)}$$

$$v_4 = F^{-1}\left(\frac{1}{S_\mathrm{r}}\right)\cdot r_z * \frac{\partial}{\partial r}\left[\begin{array}{l} c_{33}\left(F^{-1}\left(\frac{1}{S_q}\right)\mathrm{q}_z * \partial_q + F^{-1}\left(\frac{1}{S_\mathrm{r}}\right)r_z * \partial_r\right)v \\ + c_{13}\left(F^{-1}\left(\frac{1}{S_q}\right)\mathrm{q}_x * \partial_q + F^{-1}\left(\frac{1}{S_\mathrm{r}}\right)r_x * \partial_r\right)u \end{array}\right], \quad \text{(B-10)}$$

where F^{-1} and $*$ are inverse Fourier transform and convolution operators, respectively.

APPENDIX C

In the stretched-coordinate metrics, the parameters of the CPML in the q and r directions are (Komatitsch and Martin, 2007)

$$d_0 = -(N+1)\cdot\sqrt{\frac{c_{\max}}{\rho}}\cdot\frac{\log R}{2L}, \tag{C-1}$$

$$d_q = d_0\left(\frac{q}{L}\right)^N, \tag{C-2}$$

$$d_r = d_0\left(\frac{r}{L}\right)^N, \tag{C-3}$$

$$b_q = e^{-\left(\frac{d_q}{k_q}+\alpha_q\right)\cdot\Delta t}, \tag{C-4}$$

$$b_r = e^{-\left(\frac{d_r}{k_r}+\alpha_r\right)\cdot\Delta t}, \tag{C-5}$$

$$a_q = \frac{d_q}{k_q\cdot d_q + k_q^{\,2}\cdot\alpha_q}(b_q - 1), \tag{C-6}$$

$$a_r = \frac{d_r}{k_r\cdot d_r + k_r^{\,2}\cdot\alpha_r}(b_r - 1), \tag{C-7}$$

where N is a constant and equal to 2; R is the theoretical reflection coefficient, here we use 0.0001; L is the thickness of the CPML boundary; d_q and d_r are attenuation factors; q and r are the horizontal and vertical distance to the CPML boundary; a_q, a_r, b_q, and b_r are parameters used in memory variables.